Geoscience Frontiers xxx (xxxx) xxx

Contents lists available at ScienceDirect

Geoscience Frontiers

journal homepage: www.elsevier.com/locate/gsf

The Hugoniot curve and sound velocity of forsterite to 1200 GPa

Jian Song [a], Liang Sun [b], Huan Zhang [b], Xiaoxi Duan [b], Zanyang Guan [b], Lu Zhang [b], Xiaokang Feng [c], Weiming Yang [b], Hao Liu [b], Mengsheng Yang [b], Yulong Li [b], Dong Yang [b], Zhebin Wang [b], Jiamin Yang [b], Wenge Yang [c], Toshimori Sekine [c,d,e], Youjun Zhang [f], Zongqing Zhao [b], Zhongqing Wu [a,g,h,*]

[a] Laboratory of Seismic and Physics of Earth's Interior, School of Earth and Space Sciences, University of Science and Technology of China, Hefei 230026, China
[b] National Key Laboratory of Plasma Physics, Laser Fusion Research Center (LFRC), Chinese Academy of Engineering Physics, Mianyang 621900, China
[c] Center for High Pressure Science and Technology Advanced Research (HPSTAR), Shanghai 201203, China
[d] Graduate School of Engineering, Osaka University, Suita, Japan
[e] Shanghai Key Laboratory of Material Frontiers Research in Extreme Environments (MFree), Shanghai Advanced Research in Physical Sciences (SHARPS), Pudong, Shanghai 201203, China
[f] Institute of Atomic and Molecular Physics, Sichuan University, Chengdu 610065, China
[g] National Geophysical Observatory at Mengcheng, University of Science and Technology of China, Hefei 230026, China
[h] CAS Center for Excellence in Comparative Planetology, University of Science and Technology of China, Hefei 230026, China

ARTICLE INFO

Article history:
Received 8 April 2024
Revised 4 July 2024
Accepted 20 August 2024
Available online xxxx

Keywords:
Forsterite
Hugoniot
Sound velocity
First-principles molecular dynamics
Shock compression
Lateral release

ABSTRACT

The comprehension of the composition and physical state of the deep interiors of large planets, as well as the impact events pertinent to planetary formation and evolution, necessitates an understanding of the properties of planetary materials under extreme conditions. Forsterite (Mg_2SiO_4), a significant geological mineral, has not been fully characterized in terms of its behavior under shock compression due to a lack of consensus among previous experiments and simulations aimed at determining its Hugoniot, as well as the absence of knowledge of sound velocity at high pressures, a critical parameter indicative of phase transformation and melting.

In this study, we delineated the Hugoniot curve of the mineral forsterite up to immense pressures of 1200 GPa. For the first time, we successfully constrained its sound velocity along the Hugoniot curve up to 760 GPa by combining laser-driven shock experiments with first-principles molecular dynamics simulations. The measured Hugoniot data for forsterite corroborated previous findings and suggested the occurrence of incongruent melting during shock compression. Remarkably, along their respective Hugoniot curves, the sound velocity of forsterite was observed to fall between that of the minerals bridgmanite and periclase. The remarkable agreement between the experimental results and simulation data provides reliable sound velocity measurements on the forsterite Hugoniot, which is critical for comprehensively understanding the phase transition and melting behavior of forsterite under ultra-high pressures. This knowledge sheds invaluable light on the behavior of this significant geological mineral under extreme conditions akin to those found in the interiors of planets.

1. Introduction

The understanding of the behavior of geological materials under extreme conditions is crucial for elucidating the impact events during the planetary formation and uncovering the structure, composition, and evolution of large planets, such as super-Earths. Dynamic compression is the sole method capable of creating such extreme conditions (Duffy and Smith, 2019). For instance, a 10 M_E super-Earth has a core-mantle-boundary pressure of 1.3 TPa and a central pressure of approximately 4 TPa (Wagner et al., 2012). This far exceeds pressures achievable through static compression, which typically range from tens of GPa for large volume presses to hundreds of GPa for diamond anvil cell (Anzellini and Boccato, 2020; Hirao et al., 2022; Mao and Mao, 2022).

With the advancement of experimental techniques and the accomplishment of complicated loading paths, ultra-high pressure studies on geological materials have greatly progressed in recent years, primarily focusing on the equation of states (EOS), phase transitions, and melting behavior (Duffy and Smith, 2019; Li et al., 2022). For instance, the first direct structural evidence for

* Corresponding author.
E-mail address: wuzq10@ustc.edu.cn (Z. Wu).

https://doi.org/10.1016/j.gsf.2024.101917
1674-9871/

Please cite this article as: J. Song, L. Sun, H. Zhang et al., The Hugoniot curve and sound velocity of forsterite to 1200 GPa, Geoscience Frontiers, https://doi.org/10.1016/j.gsf.2024.101917

the B1-B2 phase transition in MgO was observed through *in-situ* X-ray diffraction in the ramp compression experiments (Coppari et al., 2013). The melting curve of silica under super-Earth conditions has been determined through the shock loading of fused silica, α-quartz, and stishovite (Millot et al., 2015). A reference density profile of $MgSiO_3$ mantle of super Earths up to at least 8 M_E has been updated based on high-quality density data of solid $MgSiO_3$, which was obtained from direct shockwave loading of pre-synthesized bridgmanite (Fei et al., 2021).

As another important terrestrial material, the shock-compression behavior of forsterite (Mg_2SiO_4) remains controversial. Sekine et al. (2016) conducted laser-driven shock experiments on single-crystal forsterite from 250 to 970 GPa and observed several slope changes in the U_S-U_P space and pressure–temperature (P-T) data between 270 and 470 GPa on the forsterite Hugoniot. This phenomenon was attributed to a series of complex phase transitions, including the incongruent crystallization of MgO from liquid forsterite, subsequent phase transition of solid MgO, and its melting (Sekine et al., 2016). However, due to the experimental challenges associated with these extreme conditions, exact melting scenario remained inconclusive (Bolis et al., 2016; Root et al., 2018). To understand phase transitions and melting processes, reliable simulations and direct structural observations or thermodynamic parameters measurements are essential. For instance, a sudden decrease in sound velocity suggests that forsterite may melt at approximately 150 GPa (Brown et al., 1987). Recent *in-situ* X-ray diffraction measurements have revealed that forsterite would transform into its metastable phase, forsterite III, at 30–75 GPa along the Hugoniot curve (Newman et al., 2018; Kim et al., 2021). This is due to the kinetic effect in the shock compression experiments, which inhibits the transformation of forsterite into the assemblage of bridgmanite and periclase, the stable phase under these conditions. However, there is a current lack of structural observations and sound velocity measurements and simulations above 200 GPa on the forsterite Hugoniot.

In this study, we use both the laser-driven shock experiments and first-principles molecular dynamics (FPMD) simulations to obtain the Hugoniot curve of forsterite up to 1200 GPa and report the sound velocity of forsterite along the Hugoniot curve up to 760 GPa for the first time. The agreement between experimental and computational results provide a reliable dataset for further understanding the melting properties of forsterite at ultra-high pressure.

2. Methods

2.1. Experiments

The laser-driven shock compression experiment was conducted at the Shen Guang-III prototype (SG-IIIp) laser facility (Gong et al., 2019; Lan, 2022; Fan et al., 2023), situated at the Laser Fusion Research Center (LFRC) in Mianyang, China. The SG-IIIp laser system operates at a wavelength of 351 nm, achieved through frequency tripling of Nd:glass, with 8 beams delivering 800 J of energy per beam and nanosecond pulse shaping capability, while the 9th beam provides up to 3000 J within a 3−20 ns pulse duration. In the present experiment, 8 laser beams delivered a total of 6400 J of laser energy into the hohlraum, with a 1−4 ns flat-top temporal pulse shape. An intense, uniform radiation field, generated within the hohlraum through X-ray absorption, deposited energy into the designed Al pusher, thereby generating a strong shock wave that compressed the forsterite samples up to 1.2 TPa (Liu et al., 2018; Sun et al., 2021; Wang et al., 2021). The schematic representation of the shock compression experimental setup is illustrated in Fig. 1. Detailed information regarding the targets is provided in the Supplementary data Fig. S1.

For shock Hugoniot measurements, Al and quartz were utilized as the reference standard and transparent reference, respectively, Transparent single-crystal forsterite samples with an initial density of 3.226 g/cm^3 were used in the experiment. The shock compression was performed along the <100> crystal direction, with the free sides of the forsterite sample maintained perpendicular to the shock compression direction. Anti-reflection coatings optimized for a wavelength of 532 nm were applied to the rear sample surfaces to minimize back reflections. The refractive index of forsterite at 532 nm was 1.60.

The standard line velocimetry interferometer system for any reflector (VISAR) (Celliers and Millot, 2023) with 532 nm probe laser wavelength was the primary ultrafast diagnostic. The shock front in transparent forsterite becomes reflective at above 200 GPa (Sekine et al., 2016). In the present experiments, initial shock waves in samples were strong enough. VISAR continuously tracks the optical reflecting shock front as a function of time. Fig. 1b shows the typical raw data for VISAR measurement in shot 344. When the shock breaks out from Al into the sample, the shock velocities of forsterite and quartz were measured simultaneously by line-VISAR. The particle velocity U_P was determined by the impedance-matching (IM) technique using the Hugoniot of Al and quartz and the release of Al for the reference materials (Celliers et al., 2005; Hamel et al., 2012; Sekine et al., 2016).

As the time progresses shown in Fig. 1b, the lateral release wave emanating from the free side surpasses and subsequently bends the shock fronts in a continuous manner within transparent samples, which should otherwise propagate planarly, as observed in the central regions. The trajectory of the bent location could potentially serve as an indicator of the sound velocity, utilizing the methods developed by Al'Tshuler et al. (1960) and Zel'Dovich and Raizer (2002), and proposed for implementation in laser shock experiments (Li et al., 2018; Sun et al., 2021).

The sound velocity C_S can be obtained by Eq. (1):

$$C_S = U_S \times \sqrt{\left(\tan^2\phi + (1 - U_P/U_S)^2\right)} \tag{1}$$

where U_S is the shock velocity, U_P is the particle velocity behind the shock front, and ϕ is the angle between the shock direction and the bending trace. The angle ϕ was determined by VISAR measurement, considering the spatial scaling factor M as $\phi = \tan^{-1}[(dx/M)/dy]$. Here, dx is the horizontal pixel difference between the initial and final bend positions, and dy is the travel distance when the shock propagates over a certain time interval. In the analysis, the average sound velocity for each shot was calculated using the average shock velocity, as the shock velocity U_S did not exhibit significant decay.

Two VISAR etalons with lengths of 10 mm and 7 mm were employed in two independent interferometers to constrain the integer number of base fringe shifts. The velocity sensitivities [velocity per fringe (VPF)] were obtained as 3.015 and 4.323 μm/ns/fringe for forsterite, and 3.235 and 4.639 μm/ns/fringe for quartz. The low-VPF VISAR was used for determining the final velocity value due to more precise values compared to the high-VPF VISAR. An injection-seeded, Q-switched, yttrium–aluminum garnet laser operating at a wavelength of 532 nm served as the probe laser beam for VISAR. The shock velocity histories in forsterite and quartz could be derived from the changes in the fringe pattern recorded by streak cameras. Planar regions with at least four fringes in each shot were carefully selected to ensure accurate determination of the shock velocities. The data reduction was performed using a 1D Fast Fourier Transform (FFT) analysis of the phase and intensity of the fringes (Celliers and Millot, 2023). Prior to the experiments, the nonlinear sweep rates of the streak cameras and the spatial scaling factor M=0.536 (μm/pixel) for the L-leg VISAR were calibrated. A 20-nanosecond temporal window

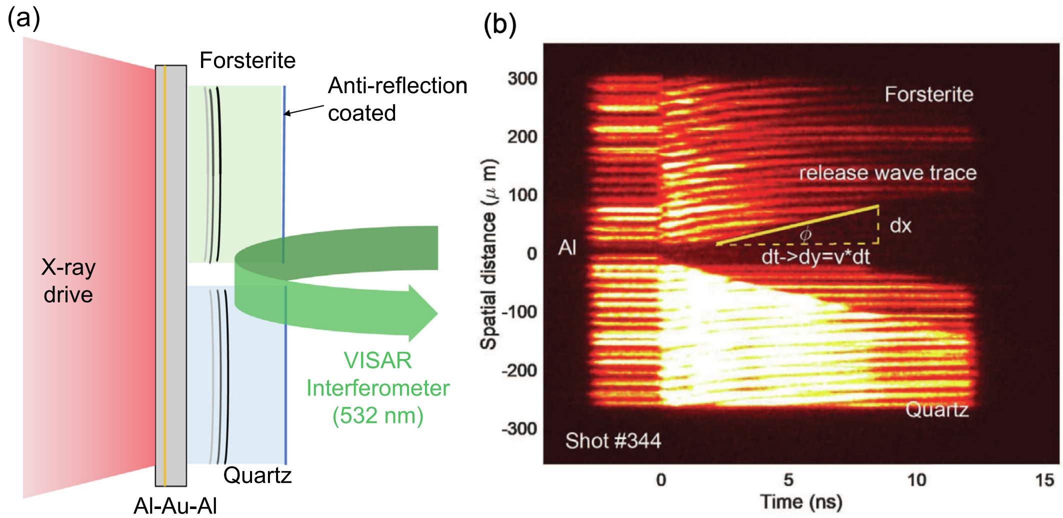

Fig. 1. Experimental setup and time-resolved measurements for dynamically compressing forsterite under shock loading. (a) Schematic of the laser shock experiment setup using VISAR line-imaging velocimetry (532 nm) to directly measure the response of forsterite (Mg_2SiO_4) and quartz (SiO_2) samples under shock compression. The samples with anti-reflection coatings were attached to an Al buffer plate with a 15 μm Al ablator layer, 5 μm Au layer, and 30 μm Al pusher to generate and tailor the shock wave. The quartz standard enables precise Hugoniot measurement, while monitoring the lateral release waves from forsterite's free surface yields its sound velocity at high pressures. (b) Typical VISAR data (Shot 344) shows the shock decay after breaking out from Al, as well as the shock fronts in forsterite, quartz, and the lateral release waves from the free sides of forsterite and quartz, captured by time-resolved line-imaging velocimetry. See Supplementary Materials for details.

was utilized by the streak cameras to detect the reflected probe signal, providing uncertainties less than approximately 1% in the shock velocity measurements. The temporal resolution was estimated for the employed streak window.

For standard material, the quartz Hugoniot we used to be $U_S = (2.40 \pm 0.10) + (1.68 \pm 0.02)U_P - (0.0155 \pm 0.0010)U_P{}^2$ (Hamel et al., 2012). And we used the Al Hugoniot as $U_s = (17.992 \pm 0.078) + (1.167 \pm 0.026)(U_P - 9.838)$ (Celliers et al., 2005). In sound velocity analysis, we used the general U_S-U_P relations to calculate U_P from the relations $U_S = 6.89 + 1.22U_P - 1.50U_P e^{-0.40U_P}$ in the ref. (Root et al., 2018). The IM interface shock velocity U_S^{Fo} for forsterite and U_S^{Q} for quartz were obtained by the extrapolation of the velocity history in 200–600 ps periods after shock break from Al standard.

The uncertainties for the Hugoniot parameters of forsterite were propagated using the Monte Carlo method based on uncertainties. One thousand datasets were randomly generated within the specified uncertainties. Random errors arise from uncertainties in the observables (shock velocities), while systematic errors originate from uncertainties in the standard materials used in experiments (quartz and Al), the precision of the various fits employed, the principal Hugoniot and release models. The systematic errors in the sound velocity measurements, stemming from the coefficients in the forsterite Hugoniot relations, the spatial scaling factor M, and the resolutions of streak cameras, primarily contribute to an uncertainty of approximately 5%. Meanwhile, the random errors associated with the selection of data points are reduced through the averaging process in the sound velocity analysis. More details for uncertainties are shown in the Supplemental Materials (Supplementary data Figs. S2-S3).

2.2. FPMD simulation details

The Hugoniot curve describes the locus of all possible shocked states from a given initial state and is governed by the Rankine-Hugoniot jump conditions (Duvall and Graham, 1977) Eqs. (2)-(4):

$$E - E_0 = \frac{1}{2}(P + P_0)\left(\frac{1}{\rho_0} - \frac{1}{\rho}\right) \quad (2)$$

$$P - P_0 = \rho_0 U_S U_P \quad (3)$$

$$\rho = \frac{\rho_0 U_S}{U_S - U_P} \quad (4)$$

where E, P, ρ, U_S, and U_P represent specific internal energy, pressure, density, shock velocity, and particle velocity, respectively, with the subscript 0 denoting the initial state. To determine the Hugoniot curve, we calculated the pressure and internal energy under varying temperatures and a given volume within the NVT ensemble, thereby establishing the *P-E-T* relationship at the given volume, from which the solution that satisfies the Eq. (2) can be determined.

The bulk sound velocity V_B can be deduced from the following thermodynamic relationship: $V_B = \sqrt{\frac{K_s}{\rho}}$, $K_s = (1 + \alpha\gamma T)K_T$, $K_T = -V\left(\frac{\partial P}{\partial V}\right)_T$, $\alpha = \frac{1}{V}\left(\frac{\partial V}{\partial T}\right)_P$, $\gamma = V\left(\frac{\partial P}{\partial E}\right)_V$, $\left(\frac{\partial P}{\partial V}\right)_T = -\frac{\left(\frac{\partial P}{\partial T}\right)_V}{\left(\frac{\partial V}{\partial T}\right)_P}$, where α, γ, K_T, and K_S represent thermal expansion, Gruneisen parameter, isotherm bulk modulus, and adiabatic bulk modulus, respectively. To calculate the sound velocity for each Hugoniot point (P^*, V^*), we calculated the pressure and internal energy under varying temperatures and the given volume within the NVT ensemble to obtain the *P-E-T* relationship at the given volume V^*, as well as the volume and internal energy under varying temperatures and the given pressure within the NPT ensemble to obtain the V-E-T relationship at the given pressure P^*. From this, the isochoric derivatives $\left(\frac{\partial P}{\partial E}\right)_V$ and $\left(\frac{\partial P}{\partial T}\right)_V$, as well as the isobaric derivative $\left(\frac{\partial V}{\partial T}\right)_P$, can be obtained, thereby enabling the derivation of thermodynamic parameters and sound velocity. The uncertainties of these properties were estimated using the block-averaging method (Flyvbjerg and Petersen, 1989) and error propagation.

First-principles molecular dynamics (FPMD) simulations were performed using the VASP with Perdew-Burke-Ernzerhof (PBE) projector-augmented wave (PAW) potentials (Kresse and Furthmüller, 1996; Perdew et al., 1996). The initial configuration is a 2 × 1 × 2 supercell of forsterite (16 Mg_2SiO_4, 112 atoms) with a density of 3.2224 g/cm^3. The gamma-point Brillouin-zone sampling was adopted. A plane wave cutoff energy of 800 eV was utilized to minimize the Pulay stress. The core radii are Mg: 1.058 Å ($2p^6 3s^2$), Si: 1.312 Å ($3s^2 3p^2$), and O: 0.820 Å ($2s^2 2p^4$). This set of

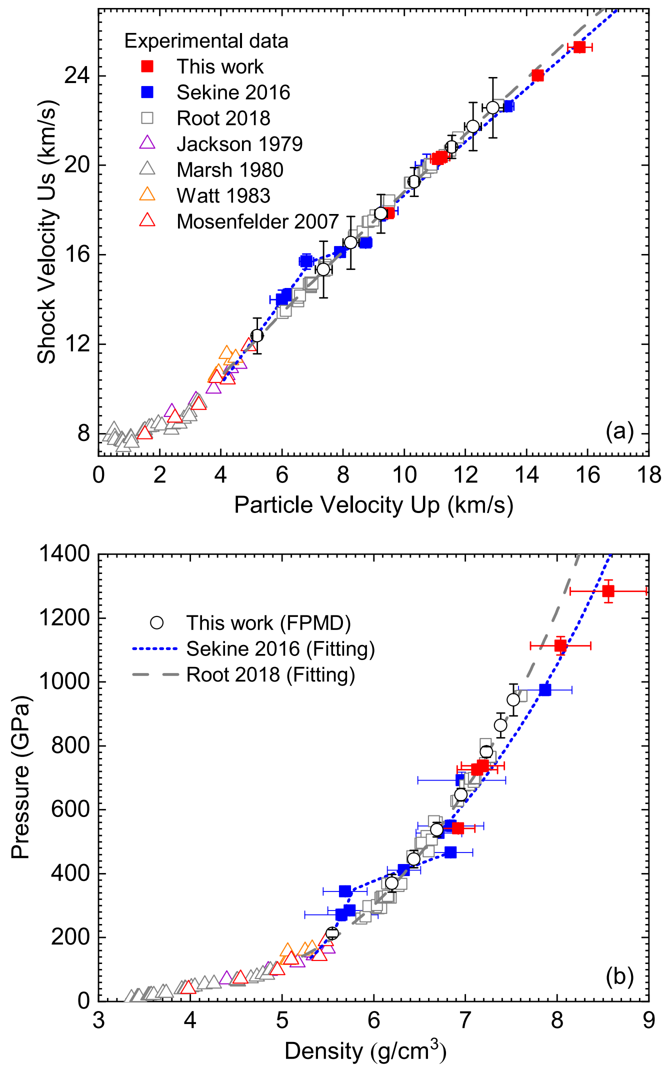

Fig. 2. The Hugoniot measurement and calculation of forsterite with error bars in the (a) Us-Up and (b) Pressure-density planes. Previous experimental data are illustrated for comparison (Jackson and Ahrens, 1979; Marsh, 1980; Watt and Ahrens, 1983; Mosenfelder et al., 2007; Sekine et al., 2016; Root et al., 2018). Our data in FPMD calculation and experimental measurement are close to the previous results in refs. (Sekine et al., 2016; Root et al., 2018).

pseudopotentials has been successfully utilized in previous studies to conduct FPMD simulations at pressures exceeding 1 TPa for $MgSiO_3$ (Fei et al., 2021) and Mg_2SiO_4 (Root et al., 2018). Thermal equilibrium between ions and electrons was assumed via the Mermin functional (Mermin, 1965). Run durations with a time step of 1 fs ranged from 5 to 10 ps, with the first 1 ps allowing the system to reach thermal equilibrium and the remaining time utilized for statistical equilibrium properties.

3. Results and discussion

3.1. The Hugoniot curve of forsterite

The measured shock Hugoniot of forsterite in both the U_S-U_P space and the pressure-density space is illustrated in Fig. 2 and summarized in Table 1. The present Hugoniot data at higher pressure (>600 GPa) agree well with the previous results (Sekine et al., 2016). Our experimental data also support a higher density at pressure above 800 GPa along Hugoniot, but the slope changes for Us-Up relation observed in the previous measurement (Sekine et al., 2016) are difficult to confirmed due to the limited data and experimental error bars in the present results.

Furthermore, we performed a series of NVT FPMD simulations at varying temperatures and a fixed density to ascertain the P-E-T relationship at the specified density (Table 2). The Hugoniot data, the solution of equation (2), were determined from the *P-E-T* relationship without extrapolation (see Table 3), thereby ensuring the reliability of our results. Our FPMD simulations yielded more consistent results with Root et al. (2018) rather than Sekine et al. (2016). The temperatures on the forsterite Hugoniot determined from FPMD simulations are generally consistent with the prior experimental results (Lyzenga and Ahrens, 1980; Bolis et al., 2016; Sekine et al., 2016; Root et al., 2018) within the certain uncertainties, illustrated in Fig. 3. The radial distribution functions, which show the presence of short-range order with no long-range order (Supplementary data Fig. S4), and mean square displace-

Table 2
Converged thermodynamic quantities and statistical standard errors from FPMD calculations.

ρ(kg/m^3)	E (MJ/kg)	T (K)	P (GPa)
3222.39	−32.50 ± 0.01	299 ± 5	6.0 ± 0.06
5550.72	−19.47 ± 0.02	3978 ± 12	205.9 ± 0.20
5550.72	−16.47 ± 0.03	5967 ± 17	222.8 ± 0.30
6198.85	−6.69 ± 0.06	8939 ± 22	356.8 ± 0.52
6198.85	−2.64 ± 0.07	10928 ± 26	381.2 ± 0.53
6437.22	−1.18 ± 0.09	10920 ± 27	423.3 ± 0.71
6437.22	4.56 ± 0.07	13903 ± 32	458.3 ± 0.57
6688.08	8.55 ± 0.08	14888 ± 34	521.4 ± 0.66
6688.08	17.53 ± 0.09	19852 ± 40	575.8 ± 0.64
6952.03	16.17 ± 0.09	17859 ± 39	612.2 ± 0.65
6952.03	28.20 ± 0.07	24801 ± 50	686.1 ± 0.55
7230.11	34.10 ± 0.11	26769 ± 54	774.2 ± 0.80
7230.11	38.81 ± 0.10	29744 ± 54	803.5 ± 0.78
7383.49	40.48 ± 0.09	29733 ± 56	844.9 ± 0.73
7383.49	50.72 ± 0.10	36159 ± 68	907.7 ± 0.75
7523.18	46.62 ± 0.10	32695 ± 58	912.2 ± 0.76
7523.18	55.99 ± 0.11	38631 ± 65	969.8 ± 0.83

Table 1
Shock Hugoniot data for forsterite in the present measurement.

Shot No.	U_S^Q (km/s)	U_S^{Fo} (km/s)	u_P^{Fo} (km/s)	P^{Fo} (GPa)	ρ^{Fo} (g/cm^3)
340	24.42 ± 0.19	24.01 ± 0.16	14.37 ± 0.13	1113.16 ± 28.94	8.04 ± 0.33
341	26.03 ± 0.19	25.27 ± 0.21	15.74 ± 0.40	1283.95 ± 35.57	8.56 ± 0.42
343	20.22 ± 0.14	20.27 ± 0.17	11.10 ± 0.24	725.95 ± 16.91	7.13 ± 0.22
344	20.38 ± 0.17	20.37 ± 0.17	11.23 ± 0.26	737.88 ± 17.93	7.19 ± 0.23
345	17.86 ± 0.11	17.86 ± 0.10	9.47 ± 0.20	541.72 ± 12.24	6.92 ± 0.18

Note: U_S^{Fo} and U_S^Q are the measured shock velocities in forsterite and quartz with measurement errors. The pressure P^{Fo}, density ρ^{Fo}, and particle velocity U_P^{Fo} are determined from the impedance-matching calculations with errors (random and systematics errors). Random errors come from measurement uncertainties in U_S^{Fo} and U_S^Q, and systematic errors come from uncertainties in the principle Hugoniot of quartz and Al and the release of Al.

Table 3
The shock Hugoniot parameters obtained by the simulations.

ρ (kg/m^3)	E (MJ/kg)	T (K)	P (GPa)	U_S (km/s)	U_P (km/s)
5550.72	−18.27 ± 1.55	4779 ± 1029	213 ± 12	12.38 ± 0.80	5.19 ± 0.15
6198.85	−4.48 ± 3.01	10025 ± 1479	370 ± 27	15.34 ± 1.27	7.36 ± 0.27
6437.22	2.51 ± 2.96	12837 ± 1539	446 ± 28	16.54 ± 1.18	8.26 ± 0.26
6688.08	11.19 ± 2.43	16350 ± 1346	537 ± 23	17.83 ± 0.86	9.24 ± 0.20
6952.03	21.89 ± 2.11	21162 ± 1219	647 ± 19	19.26 ± 0.64	10.33 ± 0.15
7230.11	35.21 ± 1.99	27551 ± 1716	781 ± 17	20.83 ± 0.51	11.55 ± 0.13
7383.49	43.57 ± 4.45	31671 ± 2799	864 ± 38	21.74 ± 1.07	12.25 ± 0.27
7523.18	51.74 ± 5.87	35938 ± 3724	944 ± 50	22.57 ± 1.34	12.90 ± 0.34

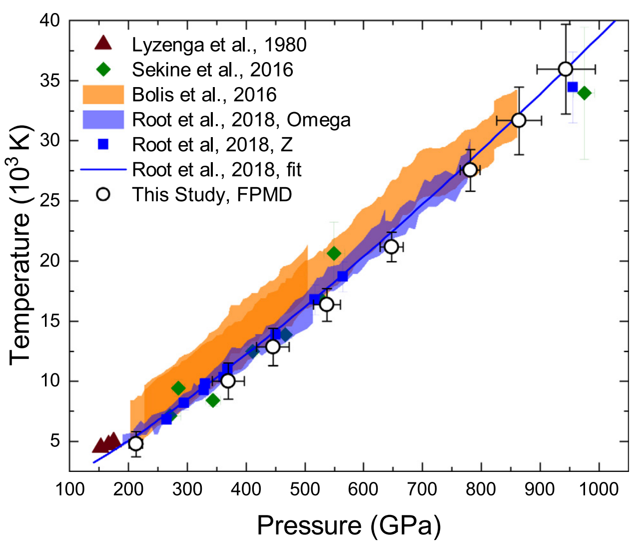

Fig. 3. The Hugoniot Pressure-Temperature for forsterite at high pressures. Previous experimental data are plotted for comparison (Lyzenga and Ahrens, 1980; Bolis et al., 2016; Sekine et al., 2016; Root et al., 2018). Our calculation in FPMD for molten forsterite is highly close to the previous measurement results in the reference (Root et al., 2018).

Table 4
Experimental measurement sound velocity of forsterite along shock Hugoniot in the present study. The total errors were considered.

Shot No.	P (GPa)	ρ (g/cm^3)	V_B (km/s)
340	695.34 ± 17.48	7.08 ± 0.00	14.91 ± 0.91
341	762.53 ± 19.31	7.22 ± 0.01	16.32 ± 0.81
344	389.38 ± 10.02	6.30 ± 0.01	13.56 ± 0.58
347	425.19 ± 11.00	6.41 ± 0.01	13.14 ± 0.60

ments, which reach the linear diffusion regime (Supplementary data Fig. S5), corroborate that forsterite has melted within our calculated *P-T* regimes along the Hugoniot curve. Consequently, the Hugoniot determined through FPMD simulations corresponds to the case of simple liquid forsterite.

3.2. Thermodynamic parameters and sound velocity of forsterite along the Hugoniot curve

The thermodynamic relationship mentioned above indicates that the accurate calculation of the derivatives, namely $\left(\frac{\partial P}{\partial E}\right)_V$, $\left(\frac{\partial P}{\partial T}\right)_V$, and $\left(\frac{\partial V}{\partial T}\right)_P$, is crucial for determining the sound velocity of liquid forsterite. For each Hugoniot data point, at least four NVT and four NPT FPMD simulations were performed to ensure the reliability of the derivatives (Supplementary data Fig. S6). The P-E points and P-T points with errors obtained within the NVT ensemble, as well as the V-T points with errors obtained within the NPT ensemble, were linearly fitted using the weighted linear regression (Thirumalai et al., 2011), from which the derivatives $\left(\frac{\partial P}{\partial E}\right)_V$, $\left(\frac{\partial P}{\partial T}\right)_V$, and $\left(\frac{\partial V}{\partial T}\right)_P$ can be deduced. The data pairs exhibit an excellent linear relationship, suggesting the derivatives are well constrained (Supplementary data Fig. S7).

The derived thermodynamic parameters, including thermal expansion α, Gruneisen parameters γ, isotherm bulk modulus K_T, and adiabatic bulk modulus K_S are reported in Fig. 4 and Table 5. The Gruneisen parameter of liquid forsterite decreases with increasing density, which has been observed in silica melt (M. Li et al., 2018) and $MgSiO_3$ melt (Millot et al., 2020). In addition, Davies et al. (2020) experimentally measured Gruneisen parameters of forsterite under released states, and their trend generally aligns with our results (see Fig. 4b).

The measured sound velocity data of forsterite along the Hugoniot up to 760 GPa is illustrated in Fig. 5 and listed in Table 4. Our sound velocity data shows a gradually increase along pressure from ~ 400 GPa to 760 GPa. Our FPMD simulations also provided the sound velocity of liquid forsterite up to 900 GPa, summarized in Table 5. The good agreement between the simulations and experimental data suggests that the FPMD simulations reproduce well the behavior of liquid Mg_2SiO_4, thereby confirming the reliability of our measured results.

Previous studies by Brown et al. (1987) measured four sound velocity points for forsterite and one sound velocity point for Fo90 olivine ($(Mg_{0.9}Fe_{0.1})_2SiO_4$). They speculated that forsterite would melt at approximately 150 GPa, based on the sudden decrease in sound velocity. Given that the addition of iron would decrease the sound velocity, the sound velocity of Fo90 olivine (the orange circle in Fig. 5) aligns with the sound velocity of liquid forsterite from FPMD simulations, suggesting the observed decrease in sound velocity in Brown et al. (1987) indeed reflects the onset melting of forsterite.

The sound velocities of bridgmanite and periclase along their respective Hugoniot curves (McCoy et al., 2019; Fei et al., 2021) are also plotted in Fig. 5 and their sound velocity-density relations are also shown in Supplementary data Fig. S8 for comparison. Along their respective Hugoniot curves, the sound velocity of forsterite (Mg_2SiO_4) lies between those of bridgmanite ($MgSiO_3$) and periclase (MgO). Furthermore, we calculated the sound velocity of bridgmanite and periclase melt using the same calculation processes, as indicated by the open blue square and green triangle in Fig. 5, respectively. These results are also consistent with the previous measurement data. Comparing the behavior for sound velocity of bridgmanite near 500 GPa as abrupt drop of sound velocity (purple and blue squares), the sound velocity data for Mg_2SiO_4 increases at pressures 40 − 190 GPa, then drops at ~ 190 GPa and continues to gradually increases at higher pressures up to 760 GPa, which indicating the melting process for shocked forsterite.

The discontinuous P-T data observed in the forsterite Hugoniot curve suggest incongruent melting or the occurrence of complex phase transitions (Sekine et al., 2016). However, the experimental

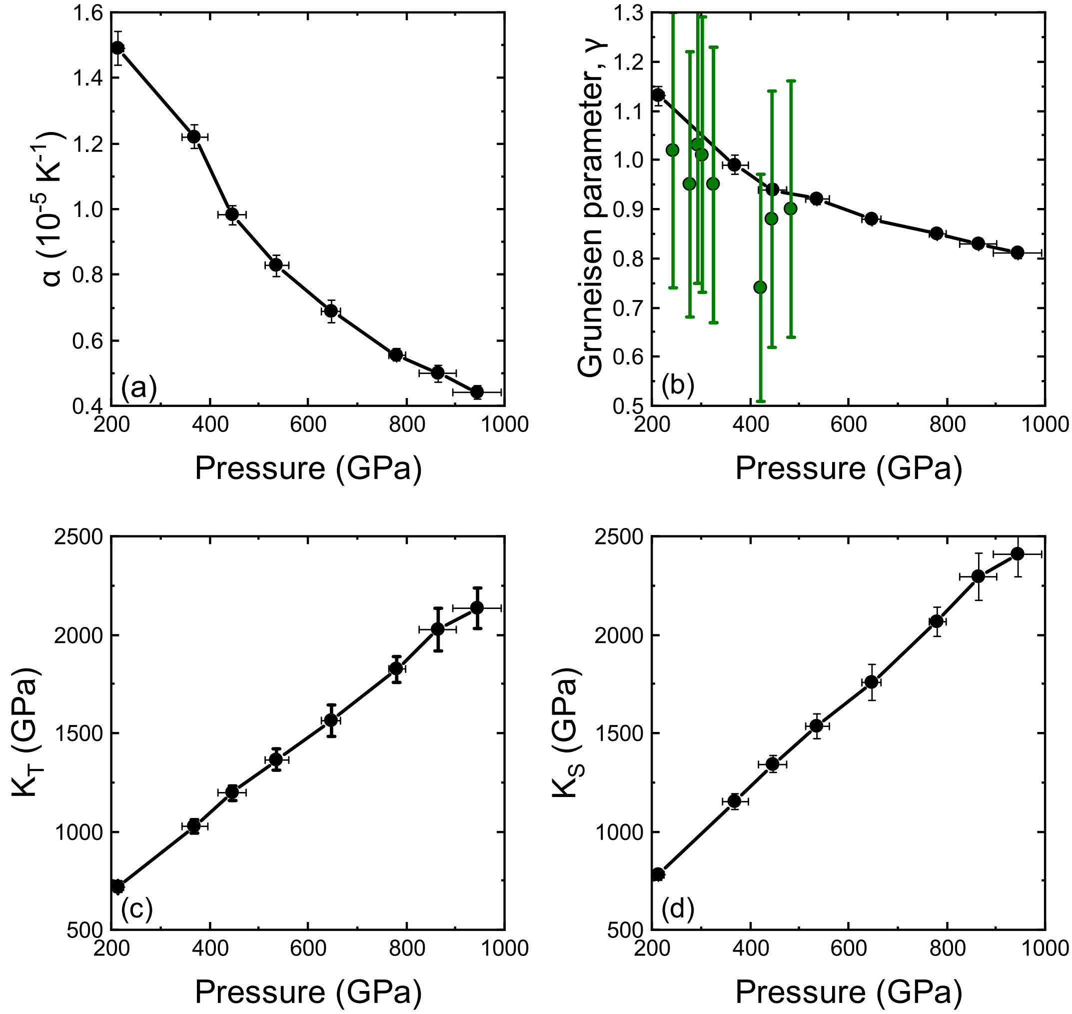

Fig. 4. Thermodynamic parameters on the forsterite Hugoniot obtained from simulations. (a) Thermal expansion α, (b) Gruneisen parameter γ, (c) isothermal bulk modulus, and (d) adiabatic bulk modulus. Experimentally measured Gruneisen parameters of forsterite under release states (green circles with vertical error bars) (Davies et al., 2020) are plotted. (For interpretation of the references to colour in this figure legend, the reader is referred to the web version of this article.)

Table 5
Shock Hugoniot data for forsterite in the present simulation. Thermal parameters and sound velocity of forsterite melt along the Hugoniot curve are obtained from FPMD simulations.

ρ (kg/m^3)	γ	α (10^{-5} K^{-1})	K_T (GPa)	K_S (GPa)	V_B (km/s)
5550.72	1.13 ± 0.02	1.49 ± 0.05	719 ± 27	780 ± 30	11.86 ± 0.23
6198.85	0.99 ± 0.02	1.22 ± 0.04	1028 ± 34	1152 ± 38	13.63 ± 0.22
6437.22	0.94 ± 0.01	0.98 ± 0.03	1196 ± 37	1341 ± 42	14.43 ± 0.23
6688.08	0.92 ± 0.01	0.83 ± 0.03	1365 ± 56	1532 ± 63	15.13 ± 0.31
6952.03	0.88 ± 0.02	0.69 ± 0.03	1561 ± 80	1759 ± 91	15.91 ± 0.41
7230.11	0.85 ± 0.01	0.56 ± 0.02	1824 ± 66	2065 ± 76	16.90 ± 0.31
7383.49	0.83 ± 0.01	0.50 ± 0.03	2026 ± 106	2293 ± 121	17.62 ± 0.46
7523.18	0.81 ± 0.01	0.44 ± 0.03	2134 ± 101	2407 ± 115	17.89 ± 0.43

uncertainties associated with the measured sound velocity in the present work limit the resolution for identifying the incongruent melting process or the phase transition components. Enhanced understanding necessitates the reduction of these uncertainties, direct *in-situ* structural measurements or additional detailed simulations for other potential components.

4. Conclusion

Sound velocity data of shocked forsterite up to 760 GPa by lateral release technique was first presented by our laser-driven shock experiment. First-principles molecular dynamics simulations, which agree well with the experimental data, were used to aid the interpretation of the observations. The measured Hugoniot data for forsterite corroborated previous findings and suggested the occurrence of incongruent melting during shock compression. The remarkable agreement on sound velocity results provides a critical constraint on melt transition of forsterite, which in turn, could impact the prospects of driving a dynamo in massive rocky planets. With emerging the *in-situ* XRD diagnostics capabilities at intense laser facilities (Coppari et al., 2013; Rygg et al., 2020) and X-ray free electron lasers (XFELs) (Makarov et al., 2023), capturing the enclosed structure evolution information for shocked forsterite

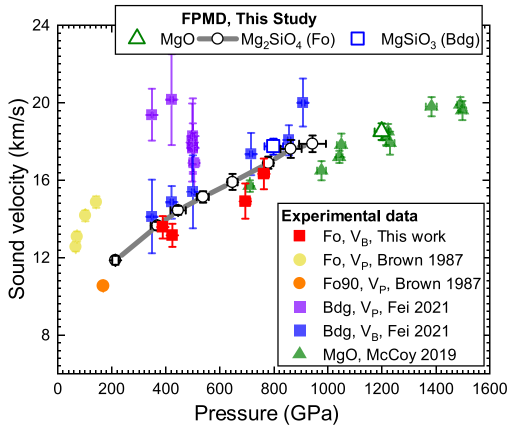

Fig. 5. Sound velocity versus pressure for Mg_2SiO_4 (Fo) compared to other silicates at high pressures. Our measured shock data (red squares) and calculated results for molten forsterite (gray circles) agree well within experimental uncertainties. The bulk sound velocities (V_B) of forsterite are slight lower than those reported for $MgSiO_3$ bridgmanite (Bdg, blue squares) from Fei et al. (2021), but higher than those for MgO periclase (green triangles) from McCoy et al. (2019) at high pressures. A sudden decrease of longitudinal velocity (V_P) tends to indicate the occurrence of melting. (For interpretation of the references to colour in this figure legend, the reader is referred to the web version of this article.)

above 200 GPa will be helpful for provide direct evidence for high-pressure silicates in the near future. Our research not only improves our understanding of the behavior of geological materials under shock compression but also provides a reliable confidence for the studying the physical properties at extreme high pressure–temperature conditions relevant to planetary interiors.

CRediT authorship contribution statement

Jian Song: Investigation, Data curation, Writing-original draft. **Liang Sun:** Conceptualization, Investigation, Data curation, Writing-original draft. **Huan Zhang:** Data curation. **Xiaoxi Duan:** Methodology. **Zanyang Guan:** Data curation, Investigation. **Lu Zhang:** Investigation, Methodology. **Xiaokang Feng:** Formal analysis. **Weiming Yang:** Investigation, Software. **Hao Liu:** Investigation. **Mengsheng Yang:** Investigation. **Yulong Li:** Data curation, Investigation. **Dong Yang:** Resources, Software. **Zhebin Wang:** Investigation, Resources, Software. **Jiamin Yang:** Project administration, Resources. **Wenge Yang:** Formal analysis, Visualization. **Toshimori Sekine:** Conceptualization, Writing-review& editing, Funding acquisition. **Youjun Zhang:** Conceptualization. **Zongqing Zhao:** Project administration, Resources. **Zhongqing Wu:** Project administration, Resources, Writing-review & editing, Funding acquisition.

Declaration of competing interest

The authors declare that they have no known competing financial interests or personal relationships that could have appeared to influence the work reported in this paper.

Acknowledgments

We thank Ji Yan, Lifeng Wang, Weichao Tong for useful and helpful discussions. We acknowledge the crucial contributions from the SGIII-prototype laser management, staff, and support team for shots and target fabrication team for providing the targets. Zhongqing Wu acknowledges the financial support from the Natural Science Foundation of China (41925017). Toshimori Sekine acknowledges the financial support from Shanghai Key Laboratory of Material Frontiers Research in Extreme Environments, China (No. 22dz2260800) and Shanghai Science and Technology Committee, China (No. 22JC1410300). Youjun Zhang acknowledges the financial support from the Sichuan Science and Technology Program (No. 2023NSFSC1910). The computations were conducted in the Supercomputing Center of the University of Science and Technology of China.

Appendix A. Supplementary material

Supplementary data to this article can be found online at https://doi.org/10.1016/j.gsf.2024.101917.

References

Al'Tshuler, L., Kormer, S., Brazhnik, M., Vladimirov, L., Speranskaya, M., Funtikov, A., 1960. The isentropic compressibility of aluminum, copper, lead, and iron at high pressures. Sov. Phys. JETP 11 (4), 766.

Anzellini, S., Boccato, S., 2020. A practical review of the laser-heated diamond anvil cell for university laboratories and synchrotron applications. Crystals 10, 459.

Bolis, R.M., Morard, G., Vinci, T., Ravasio, A., Bambrink, E., Guarguaglini, M., Koenig, M., Musella, R., Remus, F., Bouchet, J., Ozaki, N., Miyanishi, K., Sekine, T., Sakawa, Y., Sano, T., Kodama, R., Guyot, F., Benuzzi-Mounaix, A., 2016. Decaying shock studies of phase transitions in MgO-SiO_2 systems: Implications for the super-Earths' interiors. Geophy. Res. Lett. 43 (18), 9475–9483.

Brown, J.M., Furnish, M.D., Mcqueen, R.G., 1987. Thermodynamics for (Mg, Fe)$_2SiO_4$ from the hugoniot. In: Manghnani, M. H., Syono, Y. (Eds), High-pressure research in mineral physics: A volume in honor of Syuniti Akimoto. Terra Scientific Publishing Company (TERRAPUB), Tokyo, pp. 373-384.

Celliers, P.M., Millot, M., 2023. Imaging velocity interferometer system for any reflector (VISAR) diagnostics for high energy density sciences. Rev. Scientif. Instrum. 94 (1), 011101.

Celliers, P.M., Collins, G.W., Hicks, D.G., Eggert, J.H., 2005. Systematic uncertainties in shock-wave impedance-match analysis and the high-pressure equation of state of Al. J. App. Phys. 98 (11), 113529.

Coppari, F., Smith, R.F., Eggert, J.H., Wang, J., Rygg, J.R., Lazicki, A., Hawreliak, J.A., Collins, G.W., Duffy, T.S., 2013. Experimental evidence for a phase transition in magnesium oxide at exoplanet pressures. Nature Geosci. 6 (11), 926–929.

Davies, E.J., Carter, P.J., Root, S., Kraus, R.G., Spaulding, D.K., Stewart, S.T., Jacobsen, S. B., 2020. Silicate melting and vaporization during rocky planet formation. J. Geophy. Res. Planets 125 (2). e2019JE006227.

Duffy, T.S., Smith, R.F., 2019. Ultra-high pressure dynamic compression of geological materials. Front. Earth Sci. 7, 23.

Duvall, G., Graham, R., 1977. Phase transitions under shock-wave loading. Rev. Modern Phys. 49 (3), 523.

Fan, M., Lin, S., Yao, K., Qi, Y., Zhang, J., Zheng, J., Wang, P., Ni, L., Bao, X., Zhou, D., 2023. Spectrum-tailored random fiber laser towards ICF laser facility. Matter Radiat. Extremes 8 (2), 029901.

Fei, Y., Seagle, C.T., Townsend, J.P., McCoy, C.A., Boujibar, A., Driscoll, P., Shulenburger, L., Furnish, M.D., 2021. Melting and density of $MgSiO_3$ determined by shock compression of bridgmanite to 1254 GPa. Nat. Commun. 12 (1), 876.

Flyvbjerg, H., Petersen, H.G., 1989. Error estimates on averages of correlated data. J. Chem. Phys. 91 (1), 461–466.

Gong, T., Hao, L., Li, Z., Yang, D., Li, S., Li, X., Guo, L., Zou, S., Liu, Y., Jiang, X., Peng, X., Xu, T., Liu, X., Li, Y., Zheng, C., Cai, H., Liu, Z., Zheng, J., Wang, Z., Li, Q., Li, P., Zhang, R., Zhang, Y., Wang, F., Wang, D., Wang, F., Liu, S., Yang, J., Jiang, S., Zhang, B., Ding, Y., 2019. Recent research progress of laser plasma interactions in Shenguang laser facilities. Matter Radiat.t. Extremes 4 (5), 055202.

Hamel, S., Benedict, L.X., Celliers, P.M., Barrios, M.A., Boehly, T.R., Collins, G.W., Döppner, T., Eggert, J.H., Farley, D.R., Hicks, D.G., Kline, J.L., Lazicki, A., LePape, S., Mackinnon, A.J., Moody, J.D., Robey, H.F., Schwegler, E., Sterne, P.A., 2012. Equation of state of CH1.36: First-principles molecular dynamics simulations and shock-and-release wave speed measurements. Phys. Rev. B, Condensed Matt. Mater. Phys. 86 (9), 094113.

Hirao, N., Akahama, Y., Ohishi, Y., 2022. Equations of state of iron and nickel to the pressure at the center of the Earth. Matter Radiat. Extremes 7 (3), 038403.

Jackson, I., Ahrens, T.J., 1979. Shock wave compression of single-crystal forsterite. J. Geophy. Res. Solid Earth 84 (B6), 3039–3048.

Kim, D., Tracy, S.J., Smith, R.F., Gleason, A.E., Bolme, C.A., Prakapenka, V.B., Appel, K., Speziale, S., Wicks, J.K., Berryman, E.J., Han, S.K., Schoelmerich, M.O., Lee, H.J., Nagler, B., Cunningham, E.F., Akin, M.C., Asimow, P.D., Eggert, J.H., Duffy, T.S., 2021. Femtosecond X-ray diffraction of laser-shocked forsterite (Mg_2SiO_4) to 122 GPa. J. Geophy. Res Solid Earth 126 (1). e2020JB020337.

Kresse, G., Furthmüller, J., 1996. Efficient iterative schemes for ab initio total-energy calculations using a plane-wave basis set. Phys. Rev. B 54 (16), 11169.

Lan, K., 2022. Dream fusion in octahedral spherical hohlraum. Matter Radiat. Extremes 7 (5), 055701.

Li, M., Zhang, S., Zhang, H., Zhang, G., Wang, F., Zhao, J., Sun, C., Jeanloz, R., 2018. Continuous sound velocity measurements along the shock hugoniot curve of quartz. Phys. Rev. Lett. 120 (21), 215703.

Li, M., Zhang, H., Chen, S., Tao, P., Zhu, H., Zhou, C., Zhao, J., Sun, C., 2022. Laser driven dynamic compression of materials. High Power Laser Particle Beams 34 (1), 011001.

Liu, W., Duan, X., Jiang, S., Wang, Z., Sun, L., Liu, H., Yang, W., Zhang, H., Ye, Q., Wang, P., Li, Y., Yi, L., Dong, S., 2018. Laser-driven shock compression of gold foam in the terapascal pressure range. Phys. Plasmas 25 (6), 062707.

Lyzenga, G.A., Ahrens, T.J., 1980. Shock temperature measurements in Mg_2SiO_4 and SiO_2 at high pressures. Geophy. Res. Lett. 7 (2), 141–144.

Makarov, S., Dyachkov, S., Pikuz, T., Katagiri, K., Nakamura, H., Zhakhovsky, V., Inogamov, N., Khokhlov, V., Martynenko, A., Albertazzi, B., 2023. Direct imaging of shock wave splitting in diamond at Mbar pressure. Matter Radiat. Extremes 8 (6), 066601.

Mao, H.-K., Mao, W.L., 2022. Geomimicry—Liberating high-pressure research by encapsulation. Matter Radiat. Extremes 7 (6), 068102.

Marsh, S.P., 1980. LASL shock. Hugoniot data, Univ of California Press, San Francisco.

McCoy, C.A., Marshall, M.C., Polsin, D.N., Fratanduono, D.E., Celliers, P.M., Meyerhofer, D.D., Boehly, T.R., 2019. Hugoniot, sound velocity, and shock temperature of MgO to 2300 GPa. Phys. Rev. 100 (1), 014106.

Mermin, N.D., 1965. Thermal properties of the inhomogeneous electron gas. Phys. Rev. 137 (5A), A1441.

Millot, M., Dubrovinskaia, N., Černok, A., Blaha, S., Dubrovinsky, L., Braun, D.G., Celliers, P.M., Collins, G.W., Eggert, J.H., Jeanloz, R., 2015. Shock compression of stishovite and melting of silica at planetary interior conditions. Science 347 (6220), 418–420.

Millot, M., Zhang, S., Fratanduono, D.E., Coppari, F., Hamel, S., Militzer, B., Simonova, D., Shcheka, S., Dubrovinskaia, N., Dubrovinsky, L., Eggert, J.H., 2020. Recreating giants impacts in the laboratory: shock compression of bridgmanite to 14 Mbar. Geophy. Res. Lett. 47 (4). e2019GL085476.

Mosenfelder, J.L., Asimow, P.D., Ahrens, T.J., 2007. Thermodynamic properties of Mg_2SiO_4 liquid at ultra-high pressures from shock measurements to 200 GPa on forsterite and wadsleyite. J. Geophy. Res. 112 (B6), B06208.

Newman, M.G., Kraus, R.G., Akin, M.C., Bernier, J.V., Dillman, A.M., Homel, M.A., Lee, S., Lind, J., Mosenfelder, J.L., Pagan, D.C., Sinclair, N.W., Asimow, P.D., 2018. In situ observations of phase changes in shock compressed forsterite. Geophy. Res. Lett. 45 (16), 8129–8135.

Perdew, J.P., Burke, K., Ernzerhof, M., 1996. Generalized gradient approximation made simple. Phys. Rev. Lett. 77 (18), 3865.

Root, S., Townsend, J.P., Davies, E., Lemke, R.W., Bliss, D.E., Fratanduono, D.E., Kraus, R.G., Millot, M., Spaulding, D.K., Shulenburger, L., Stewart, S.T., Jacobsen, S.B., 2018. The principal hugoniot of forsterite to 950 GPa. Geophy. Res. Lett. 45 (9), 3865–3872.

Rygg, J.R., Smith, R.F., Lazicki, A.E., Braun, D.G., Fratanduono, D.E., Kraus, R.G., McNaney, J.M., Swift, D.C., Wehrenberg, C.E., Coppari, F., Ahmed, M.F., Barrios, M.A., Blobaum, K.J.M., Collins, G.W., Cook, A.L., Di Nicola, P., Dzenitis, E.G., Gonzales, S., Heidl, B.F., Hohenberger, M., House, A., Izumi, N., Kalantar, D.H., Khan, S.F., Kohut, T.R., Kumar, C., Masters, N.D., Polsin, D.N., Regan, S.P., Smith, C. A., Vignes, R.M., Wall, M.A., Ward, J., Wark, J.S., Zobrist, T.L., Arsenlis, A., Eggert, J. H., 2020. X-ray diffraction at the national ignition facility. Rev. Scient. Instrum. 91 (4), 043902.

Sekine, T., Ozaki, N., Miyanishi, K., Asaumi, Y., Kimura, T., Albertazzi, B., Sato, Y., Sakawa, Y., Sano, T., Sugita, S., Matsui, T., Kodama, R., 2016. Shock compression response of forsterite above 250 GPa. Sci. Adv. 2 (8), e1600157.

Sun, L., Zhang, H., Guan, Z., Yang, W., Zhang, Y., Sekine, T., Duan, X., Wang, Z., Yang, J., 2021. Sound velocity measurement of shock-compressed quartz at extreme conditions. Minerals 11 (12), 1334.

Thirumalai, K., Singh, A., Ramesh, R., 2011. A MATLAB™ code to perform weighted linear regression with (correlated or uncorrelated) errors in bivariate data. J. Geol. Soc. India 77 (4), 377–380.

Wagner, F.W., Tosi, N., Sohl, F., Rauer, H., Spohn, T., 2012. Rocky super-Earth interiors structure and internal dynamics of CoRoT-7b and Kepler-10b. A & A 541, A103.

Wang, P., Zhang, C., Jiang, S., Duan, X., Zhang, H., Li, L., Yang, W., Liu, Y., Li, Y., Sun, L., Liu, H., Wang, Z., 2021. Density-dependent shock Hugoniot of polycrystalline diamond at pressures relevant to ICF. Matter Radiat. Extremes 6 (3), 035902.

Watt, J.P., Ahrens, T.J., 1983. Shock compression of single-crystal forsterite. J. Geophy. Res. Solid Earth 88 (B11), 9500–9512.

Zel'Dovich, Y. B., Raizer, Y. P., 2002. Physics of shock waves and high-temperature hydrodynamic phenomena, Dover Publications,Courier Corporation.